Kinetic analysis of RNA cleavage by coronavirus Nsp15 endonuclease: Evidence for acid–base catalysis and substrate-dependent metal ion activation

Tong Huang[‡], Kimberly C. Snell[‡], Nidhi Kalia[‡], Shahbaz Gardezi, Lily Guo, and Michael E. Harris[*]
From the Department of Chemistry, University of Florida, Gainesville, Florida, USA

Reviewed by members of the JBC Editorial Board. Edited by Karin Musier-Forsyth

Understanding the functional properties of severe acute respiratory syndrome coronavirus 2 nonstructural proteins is essential for defining their roles in the viral life cycle, developing improved therapeutics and diagnostics, and countering future variants. Coronavirus nonstructural protein Nsp15 is a hexameric U-specific endonuclease whose functions, substrate specificity, mechanism, and dynamics are not fully defined. Previous studies report that Nsp15 requires Mn^{2+} ions for optimal activity; however, the effects of divalent ions on Nsp15 reaction kinetics have not been investigated in detail. Here, we analyzed the single- and multiple-turnover kinetics for model ssRNA substrates. Our data confirm that divalent ions are dispensable for catalysis and show that Mn^{2+} activates Nsp15 cleavage of two different ssRNA oligonucleotide substrates but not a dinucleotide. Biphasic kinetics of ssRNA substrates demonstrates that Mn^{2+} stabilizes alternative enzyme states that have faster substrate cleavage on the enzyme. However, we did not detect Mn^{2+}-induced conformational changes using CD and fluorescence spectroscopy. The pH-rate profiles in the presence and absence of Mn^{2+} reveal active-site ionizable groups with similar pK_as of ca. 4.8 to 5.2. An Rp stereoisomer phosphorothioate modification at the scissile phosphate had minimal effect on catalysis supporting a mechanism involving an anionic transition state. However, the Sp stereoisomer is inactive because of weak binding, consistent with models that position the nonbridging phosphoryl oxygen deep in the active site. Together, these data demonstrate that Nsp15 employs a conventional acid–base catalytic mechanism passing through an anionic transition state, and that divalent ion activation is substrate dependent.

In addition to the structural proteins of its viral envelope, coronaviruses encode multiple nonstructural proteins (Nsp1–16). Nsps have diverse biophysical and enzymatic activities enabling them to function in viral gene expression and replication, remodel the intracellular environment, and evade host immune responses (1–3). There has been significant progress in determining high-resolution structures of severe acute respiratory syndrome coronavirus 2 (SARS-CoV-2) Nsps, and their basic enzymatic and biochemical functions are defined. However, the molecular details of their interactions, dynamics, and regulation during the complex gene expression necessary for the viral life cycle are only beginning to emerge. An important challenge, therefore, is to understand how the catalytic mechanisms, substrate specificities, interactions, and dynamics of Nsps enable their coordinated function in infection and pathogenesis.

Multiple Nsps assemble into the replication–transcription complex (RTC) that localizes to double-membrane vesicles known as replication organelles, which provide the environment for replication and transcription of viral RNA (4–6). The function of the RTC depends on an RNA-dependent RNA polymerase (Nsp12 and cofactors Nsp7 and 8), an RNA helicase (Nsp13), and two methyltransferases (Nsp14 and 16 and cofactors Nsp10 and 9) involved in RNA capping (4, 7, 8). In addition, two ribonucleases, Nsp14 and Nsp15, are also contained in the RTC, which raises important questions regarding their functional roles, substrate specificities, and regulation or their RNA-cleaving activity (9). Nsp14 is a bifunctional enzyme that acts as an exonuclease while also containing an N7-methyltransferase domain. Together, these activities are believed to function in RNA capping and polymerase error correction (9, 10). Nsp15 is an endoribonuclease of the EndoU class that contributes to viral RNA synthesis and is also important for evading the activation of host immune responses (9, 11–13). However, its interactions with other Nsps, role in RTC function, and contributions to suppressing innate immunity are still being defined.

Nsp15 has broad substrate specificity for both ssRNA and dsRNA, and like other members of the EndoU class of ribonucleases, it characteristically cleaves 3′ of U residues by 2′-O-transphosphorylation (Fig. 1) (9, 14–19). High-resolution structures of Nsp15 bound to nucleotide and oligonucleotide substrates show that nucleobase specificity is due to H-bonding between uridine nucleobase O2 and N3 positions and conserved active-site residues S294 and N278 (14, 20, 21). To identify Nsp15 cleavage sites in host and viral RNAs, mouse macrophage cells were infected with the coronavirus mouse hepatitis virus encoding either native or an inactive mutant of Nsp15 (22). The authors observed differences in

‡ These authors contributed equally to this work.
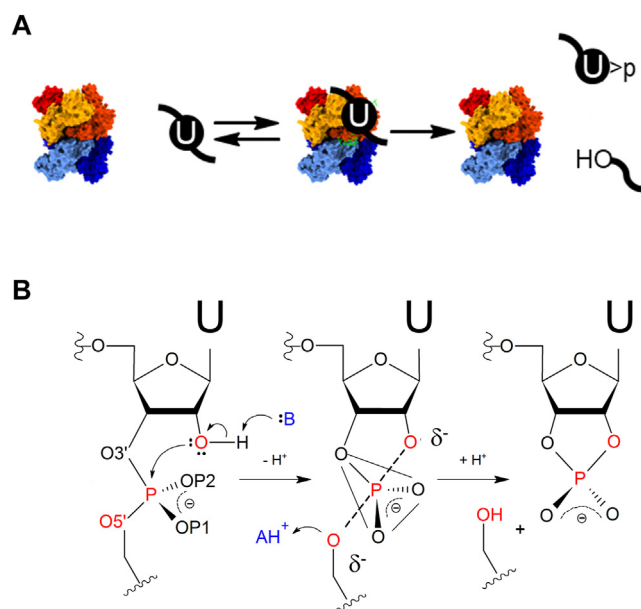* For correspondence: Michael E. Harris, harris@chem.ufl.edu.

A

B

Figure 1. Single turnover reaction and proposed mechanism of Nsp15. *A*, single-turnover kinetic scheme for cleavage of an oligonucleotide substrate by Nsp15. The diagram indicates conditions of excess enzyme resulting in binding of a model substrate (*black line*) to a single active site in the Nsp15 hexamer. The Nsp15 catalyzes RNA 2′-*O*-transphosphorylation 3′ to the uridine bound in the active site (circled U) resulting in 2′3′-cyclic phosphate and 5′-hydroxyl termini on the 5′ and 3′ cleavage products, respectively. *B*, RNA 2′-*O*-transphosphorylation reaction showing an idealized transition state that is a dianionic pentavalent phosphorane in a trigonal bipyramidal geometry with nucleophile O2′ and leaving group O5′ ligands occupying apical positions with negative charge delocalized between the O2′, O5′, and nonbridge phosphoryl oxygens. Nsp, nonstructural protein.

cyclic phosphate complementary DNA sequencing results that were compared to survey Nsp15 specificity. Motif analysis showed a preference for A 3′ to the cleavage site uridine but did not otherwise reveal an extended sequence recognition motif for Nsp15 recognition. *In vitro* biochemical studies show that Nsp15 can cleave unpaired U residues within dsRNA, demonstrating that RNA structure is likely to contribute to its biological specificity (9). Cryo-EM structures of ssRNA and dsRNA bound to Nsp15 do not show extensive contact with the surface of the enzyme (14, 21), although complexes with optimized or validated physiological substrates remain to be defined. In this regard, the impact of RNA structure, cooperativity, binding site context, and competition between alternative substrates confound a simple interpretation of motif analysis for understanding RNA-binding protein specificity (23, 24). To date, the range of physiologically relevant targets of Nsp15 have not been defined, and currently, we lack a comprehensive and quantitative understanding of Nsp15 catalytic mechanism and alternative substrate specificity.

Further complicating the picture of Nsp15 function is the potential for allosteric communication between the active sites among its six monomeric subunits (21, 25–27). The Nsp15 monomer is composed of a catalytic EndoU domain and two regions involved in hexamerization, the N-terminal domain and the middle domain. Cryo-EM reconstruction analyses of the apo form of an active-site mutant of Nsp15 revealed a high degree of

flexibility in the EndoU domain (21). Unconstrained molecular dynamics simulations of hexamer and monomer states of Nsp15 were consistent with available structural data and showed a greater degree of dynamics in the monomer and flexibility of substrate residues flanking the cleavage site (14). Moreover, previous studies of Nsp15 multiple-turnover kinetics show apparent cooperativity consistent with substrate activation (28). The potential for complex reaction kinetics suggests that the flexibility and dynamics of Nsp15 may contribute to binding, specificity, or catalysis. Complex multiple-turnover kinetics could also arise because of multiple alternative factors including the formation of multiple alternative enzyme states, hysteresis, or intermolecular interactions between substrates. A quantitative analysis of reaction kinetics is necessary to help resolve how Nsp15 *in vitro* reaction kinetics and function are related.

Previous studies reported that *in vitro* catalytic activity of Nsp15 is either dependent or enhanced by millimolar concentrations of divalent ions with Mn^{2+} (29, 30). However, activation is observed at relatively high concentrations of ions (>1 mM) compared with *in vivo* concentrations of Mn^{2+} (10–100 μM) (31, 32). To date, no evidence for metal ions in the active site has been reported for X-ray and cryo-EM structures of Nsp15, and ion-binding sites are not readily identified elsewhere in the structure. Active-site histidine residues H235 and H250 are positioned in the active site to function in acid–base catalysis of RNA 2′-*O*-transphosphorylation similar although not identical to RNase A (Fig. 1*B*). The metal ion–independent catalytic mechanism is likely based on structures with substrates carrying 2′-deoxy-modifications or uridine monophosphate (UMP)–vanadate transition state mimic (18, 20, 21). Thus, divalent ions appear to affect substrate binding or enzyme or substrate conformations in some manner, but the specific role that divalent metal ions play in Nsp15 function is not well understood.

Results

Mn^{2+} activates Nsp15 for cleavage of oligonucleotide substrates

To investigate the catalytic mechanism and role of metal ions in Nsp15 function, we used single-turnover kinetics to monitor the rate of substrate cleavage in the enzyme–substrate (ES) complex (33). Single turnover conditions ensure that only a single active site per Nsp15 hexamer on average will be occupied and thereby minimize the effects of potential allosteric communication between monomer active sites on reaction kinetics. The observed rate constant under these conditions of excess enzyme and limiting substrate depends on the fraction of S bound to Nsp15 and the rate constant for catalysis, k_c (Figs. 1 and 2). Therefore, we can quantify Nsp15

$$E + S \underset{k_{-1}}{\overset{k_1}{\rightleftharpoons}} E{\cdot}S \overset{k_c}{\longrightarrow} E{\cdot}P1{\cdot}P2$$
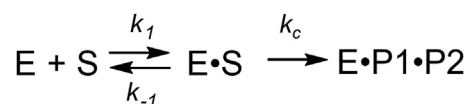
Figure 2. Single turnover reaction scheme for Nsp15. Binding of an Nsp15 active site (E) to an RNA subsrate (S) results in formation of the catalytic E•S complex. Catalysis with rate constant k_c results in cleavage products P1 and P2.

Table 1
Sequences of PUN and 1S RNA oligonucleotide substrates

PUN	Fl-U.U.U.U.U.U.U.U.U.U.G.U.C.A.U.U. C.U.C.C.U.A.A.G.A.A.G.C-Cy5
1S	Cy3-A.C.C.C.A.A.A.A.U/G.G.A. C.C.G.G.G.C.G.G.G
1S PR	Cy3-A.C.C.CA.A.A.A.U/ G.G.A.C.C.G.G.G.C.G.G.G-BHQ

catalysis by measuring k_c at saturating enzyme concentrations while the second-order rate constant k_c/K_S (where $K_S = k_{-1}/k_1$) at subsaturating enzyme concentrations.

Using this approach, we analyzed the cleavage kinetics of an oligonucleotide substrate termed 1S (Table 1). A time course of Nsp15 cleavage of 1S RNA analyzed by PAGE results shows accumulation of a single 9 nt cleavage product as expected for cleavage at the single U residue (Fig. 3). Two active-site mutants, H250A and H235A, did not show U-specific cleavage activity, and there was minimal change in substrate concentration over the same time course (Fig. S1).

In the presence of 5 mM Mn^{2+}, the single-turnover reaction kinetics of 1S cleavage were biphasic and fit to a double exponential function with rate constants of 0.05 min^{-1} and 0.3 min^{-1} for the observed slow (k_{obs1}) and fast (k_{obs2}) phases, respectively (Fig. 3C). At Nsp15 concentrations of 500 nM in the absence of divalent ions and 1 mM EDTA, Nsp15 is highly active and the k_c for cleavage of 1S is 0.03 min^{-1}. In contrast to reactions containing Mn^{2+}, the data fit to a single exponential in the absence of metal ions consistent with simple first-order kinetics (Fig. 3D). Notably, the rate constant measured in 1 mM EDTA is similar in magnitude to the rate constant for the slow reaction phase observed in the presence of Mn^{2+}. Increasing the Nsp15 concentration to 3 μM did not significantly increase the observed rate constant, demonstrating saturating enzyme concentrations in the presence and absence of metal ions (Table S1). Thus, Mn^{2+} is not essential for catalysis *per se* but nonetheless accelerates the rate constant for conversion of ES to EP (k_c in Fig. 2).

Next, we compared the single-turnover kinetics for Nsp15 cleavage of PUN (polyuridine negative-sense RNA), a model *in vivo* substrate containing a 5′ polyU leader and multiple internal uridines that was described previously (Table 1 and Fig. 4) (13, 14). The PUN RNA was 5′ end labeled with fluorescein and 3′ end labeled with Cy5 allowing visualization of both 5′ and 3′ cleavage products. As expected, based on the previous results, Nsp15 cleaves at multiple sites in the PUN RNA, and a complex pattern of products is observed. In general, the initial cleavage products appear to occur near the 5′ end within the polyU leader, evidenced by the relative sizes of the 5′ and 3′ cleavage products. The multiple initial cleavage sites and recleavage of products makes it problematic to assign rate constants to single sites by analyzing product accumulation. Therefore, to quantify k_c for the first cleavage event on an individual substrate, we analyzed the kinetics of substrate depletion (F = $[S]/([S]_{MAX}$) *versus* time). In reactions containing 5 mM Mn^{2+}, we observe biphasic kinetics for PUN similar to the 1S substrate with observed slow and fast rate constants (Fig. 4B). Data fitting showed a k_{obs1} of 0.36 min^{-1}, whereas the rate constant of the fast phase was difficult to measure accurately although a lower limit based on estimated $t_{1/2}$ is >1 min^{-1} (Table 2). In the absence of divalent ions and in the presence of 1 mM EDTA, the PUN substrate is also readily cleaved by Nsp15 like the 1S substrate with monophasic kinetics and a ~40-fold slower rate constant (k_c = 0.032 min^{-1}) (Fig. 4C).

The biphasic kinetics observed for 1S and PUN substrates in the presence of Mn^{2+} are consistent with two parallel reaction channels. This reaction mechanism could arise because of different ground state substrate conformations, two alternative conformations, or states of the ES complex. Since the rate constants for the fast and slow phases are both relatively slow (>0.1 s^{-1}) compared with RNase A and RNase T1, for example (34, 35), the two phases are unlikely to be caused by differences in association rate constants, and more likely bound and free substrates are exchangeable over the time course of the
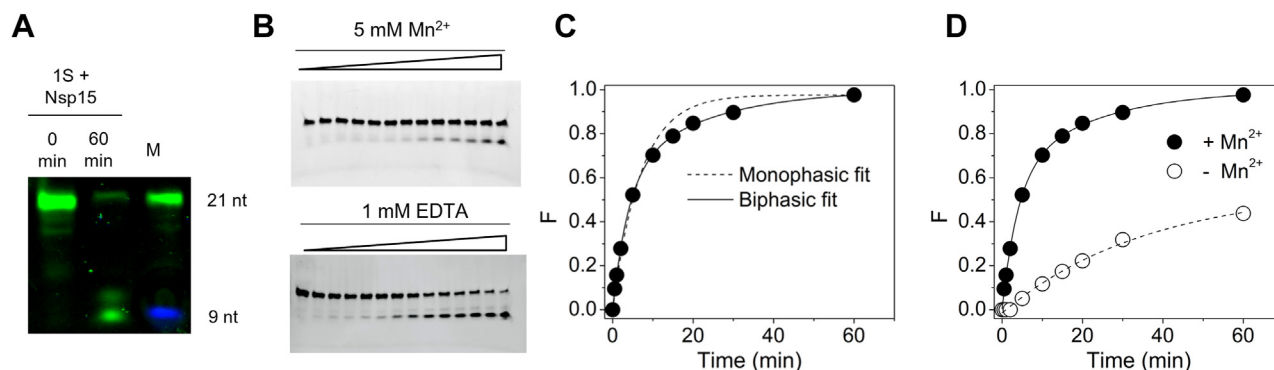

Figure 3. Single-turnover kinetics of 1S RNA cleavage by Nsp15 in the presence and absence of Mn^{2+}. *A*, comparison of 1S cleavage product to synthetic RNA standards. Single-turnover reaction time points (0 and 60 min) are run next to 21 nt and 9 nt marker RNA oligonucleotides 5′ end labeled with Cy3 and fluorescein, respectively. *B*, analysis of 1S RNA cleavage kinetics by denaturing PAGE. Time courses of Nsp15 reactions containing 0.5 μM Nsp15, 50 nM 1S, and standard reaction buffer with 5 mM Mn^{2+} or 1 mM EDTA. *C*, plot showing fraction product formed (F = ([P]/([P] + [S])) *versus* time for 1S cleavage in 5 mM Mn^{2+}. Data are fit to a single exponential (*dashed line*) or a double exponential function (*solid line*) as described in the Experimental procedures section. *D*, plot showing fraction product formed (F = ([P]/([P] + [S])) *versus* time in reactions containing 5 mM Mn^{2+} (*filled circles*) or 1 mM EDTA (*open circles*). Data for the 5 mM Mn^{2+} reaction are fit to a double exponential as shown in *B* (*solid line*). The data for the 1 mM EDTA reaction are fit to a single exponential (*dashed line*). Nsp, nonstructural protein.
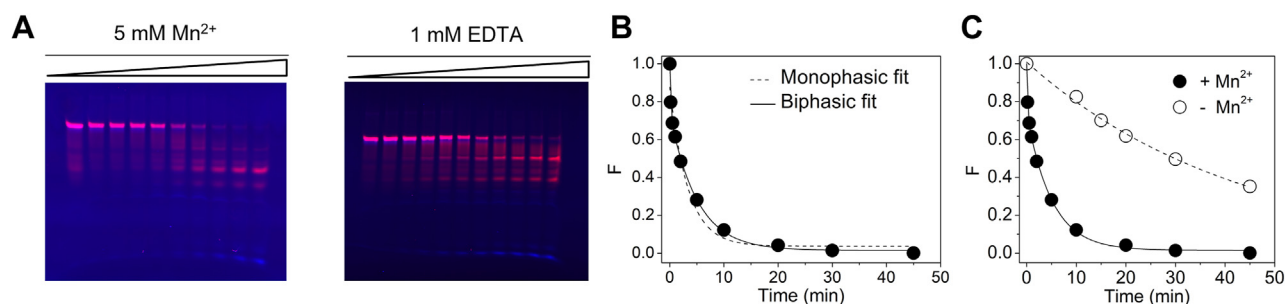
Figure 4. Single-turnover kinetics of PUN substrate RNA cleavage by Nsp15 in the presence and absence of Mn^{2+}. *A*, analysis of PUN RNA cleavage by denaturing PAGE. Time courses of Nsp15 reactions containing 0.5 µM Nsp15, 25 nM PUN, and standard reaction buffer with 5 mM Mn^{2+} or 1 mM EDTA. *B*, plot showing fraction substrate consumed (F = ([S]/([P] + [S])) *versus* time for PUN cleavage in 5 mM Mn^{2+}. Data are fit to a single exponential (*dashed line*) or a double exponential function (*solid line*). *C*, plot showing fraction substrate consumed (F = ([S]/([P] + [S])) *versus* time in reactions containing 5 mM Mn^{2+} (*filled circles*) or 1 mM EDTA (*open circles*). Data for the 5 mM Mn^{2+} reaction are fit to a double exponential as shown in *B* (*solid line*). The data for the 1 mM EDTA reaction are fit to a single exponential (*dashed line*). Nsp, nonstructural protein.

reaction. Since monophasic kinetics are observed in the absence of Mn^{2+} for both substrates, it is also unlikely that biphasic kinetics are due to a specific sequence context or conformation of the free substrate. Thus, a general model involving two alternative and slowly exchanging states of Nsp15 can describe observed biphasic reaction profile (Figs. 1 and 5).

In this model, Nsp15 exists in an ensemble of native states (ES) with similar rates of substrate cleavage k_c corresponding to k_{obs1} and therefore reacts with monophasic kinetics. Mn^{2+} stabilizes one or more states of the enzyme (E′S) that manifest a ~10-fold greater rate constant for catalysis (k'_c) corresponding to the fast phase measured by k_{obs2}. Since the reactions are measured at saturating enzyme concentration, the observed rate constant is minimally affected by the equilibrium constant for substrate binding K_s. For this reason, the differences in observed reaction kinetics do not provide information on the effects of Mn^{2+} on substrate affinity. Because the rate constants for the fast and slow phases are both relatively slow (<1 min^{-1}), equilibration between the fast- and slow-reacting ES complexes according to K_E must also be slow on the time scale of the reaction.

Previous studies reported that Mn^{2+} induced conformational changes in Nsp15 that were measurable by changes in intrinsic tryptophan fluorescence (29). Nsp15 contains three tryptophan residues per monomer, and upon excitation at 295 nm, has a broad emission spectrum with λ_{max} of approximately 340 nm (Fig. S2) (36, 37). Unlike previous reports, we do not observe changes in the tryptophan emission spectrum of Nsp15 at the low Mn^{2+} concentration (5 mM) required to observe complete

activation of cleavage for the PUN and 1S substrates. However, at high concentrations (>20 mM), a decrease in emission intensity is observed. To further examine the effects of Mn^{2+} on Nsp15 structure, we measured its CD spectrum in the presence and absence of divalent ions. The CD spectra are essentially identical with prominent negative signal at 222 nm, consistent with the large α-helical content of the folded protein (38), and no significant net change in secondary structure was induced by Mn^{2+}. The contribution of Mn^{2+} to Nsp15 catalysis is clearly distinct from divalent metal ion–dependent endonucleases and phosphohydrolases that employ essential metal ion cofactors. The overall effect observed for 1S and PUN is small compared with the overall 10^8–10^9 fold rate enhancement provided by Nsp15 in the absence of divalent ions relative to nonenzymatic RNA 2′-O-transphosphorylation (3 × 10^{-10} min^{-1} nonenzymatic rate constant (39, 40) *versus* Nsp15 single turnover k_c of 0.03 min^{-1}) (Table 2). Therefore, although intrinsic tryptophan fluorescence and CD do not provide high-resolution information, the effect of Mn^{2+} on protein structure appears to be subtle.

Since Nsp15 is stimulated by Mn^{2+} to cleave the 1S and PUN substrates, yet divalent ions are not observed in the active site, we reasoned that interactions outside the active site are most likely to drive metal ion activation. To test this premise, we analyzed the single-turnover cleavage rate for a dinucleotide substrate (pUpG) amenable to mechanistic studies of RNA 2′-O-transphosphorylation (Fig. 6) (41). Reaction kinetics were quantified by 5′ end labeling of UpG with ^{32}P and separation of 5′-^{32}P-UpG and product 5′-^{32}P-Up using denaturing PAGE and isotopic counting by phosphorimager analysis. In contrast to the PUN and 1S oligonucleotide substrates, the kinetics of pUpG cleavage in 5 mM Mn^{2+} are not biphasic but fit a single exponential function (Fig. 6B). Also, the k_{obs} increased linearly up to 10 µM enzyme concentration, whereas the k_c for oligonucleotide substrates PUN and 1S is saturated at lower (<1 µM) concentrations of Nsp15 (Fig. 6C). These data demonstrate a higher apparent K_s for a dinucleotide substrate relative to ssRNA; therefore, we quantified the effect of Mn^{2+} by measuring the second-order rate constant for pUpG cleavage (k_c/K_s in Fig. 2). The slope of a plot of k_{obs} *versus* enzyme concentration fits a linear function yielding a slope of k_c/K_s of ~2600 M^{-1} min^{-1}. Unlike 1S and PUN substrates,

Table 2

Effect of Mn^{2+} on Nsp15 catalysis for dinucleotide and ssRNA substrates

Substrate	1 mM EDTA	5 mM Mn^{2+}	
	k_c (min^{-1})	$k_{c,1}$ (min^{-1})	$k_{c,2}$ (min^{-1})
PUN	0.032 ± 0.003	0.36 ± 0.06	>1
1S	0.05 ± 0.02	0.08 ± 0.04	0.41 ± 0.15
UpG	0.04 (0.48 µM)	—	0.06 (0.48 µM)

Rate constants for Nsp15 cleavage of the substrates are listed in the first column. For 1 mM EDTA, a single rate constant for a monophasic reaction is reported. For 5 mM Mn^{2+}, the rate constants for the fast and slow kinetic phases are reported. For the PUN substrate, the fast rate constant is estimated based on a half-life of less than 1 min.
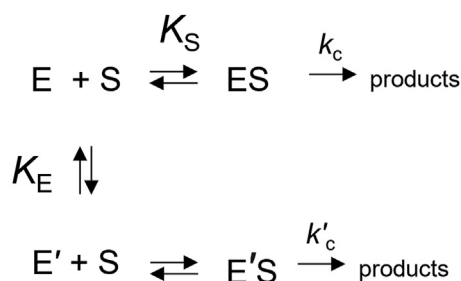
Figure 5. General model for two alternative slowly exchanging Nsp15 metal ion–dependent states. The ensemble of native states (E) and an alternative metal ion dependent state (E′) in slow exchange described by K_E bind an RNA substrate (S) with dissociation constant K_s to form ES and E′S, respectively. ES continues to react with rate constant k_c, while the E′S complex promoted by Mn^{2+} reacts with a faster rate constant k'_c.

concentrations up to 20 mM Mn^{2+} had no effect on the k_c/K_s for the single-turnover cleavage of pUpG by Nsp15. A simple interpretation is that Mn^{2+} does not contribute to either binding or catalysis for the minimal substrate. Alternatively, it is possible that the k_c/K_s measured for pUpG cleavage reflects a different rate-limiting step relative to k_c measured for the oligonucleotide substrates 1S and PUN. Nonetheless, Nsp15 is highly active in the absence of metal ions for all three alternative substrates tested (1S, PUN, and UpG; Table 2), and there is only a relatively modest effect (10-fold) of Mn^{2+} for 1S and PUN consistent with no direct role in transition state stabilization.

pH dependence of Nsp15 cleavage is consistent with a general acid–base catalytic mechanism

The analysis of pH-rate profiles can provide insight into the number and catalytic roles of ionizable functional groups in ribonuclease- and ribozyme-catalyzed RNA-2′-*O*-trans-phosphorylatoin reaction (42). Accordingly, to better understand the contribution of Mn^{2+} to Nsp15 function, we determined the effect of pH on the fast- and slow-rate reaction phases measured for cleavage reactions using the 1S substrate under single-turnover conditions (Fig. 7, *A* and *B*). We observe that the magnitudes of both k_{obs1} and k_{obs2} are sensitive to pH and increase from pH 4 to 6 and then decrease at higher pH with a plateau at approximately pH 5. This behavior is consistent with changes in protonation state of one or more functional groups engaged in proton transfer (43–45). The pH-rate profile for both k_{obs1} and k_{obs2} was fit to a simple model that assumes two active-site ionizable groups with one acting as an acid (HA^+) and the other as a base (B^-) with similar pK_a values for $pK_{a,A}$ and $pK_{a,B}$, of 5.2 and 4.8 for k_{obs1} and k_{obs2}, respectively (Fig. 7C).

Similarly, the pH dependence of Nsp15 cleavage of the dinucleotide substrate should reflect this same mechanism; however, the rate of pUpG cleavage is faster than for 1S and PUN under the same conditions. Thus, measuring rates of Nsp15 cleavage of pUpG at a pH lower than 7 by manual pipetting becomes problematic. Therefore, to investigate the
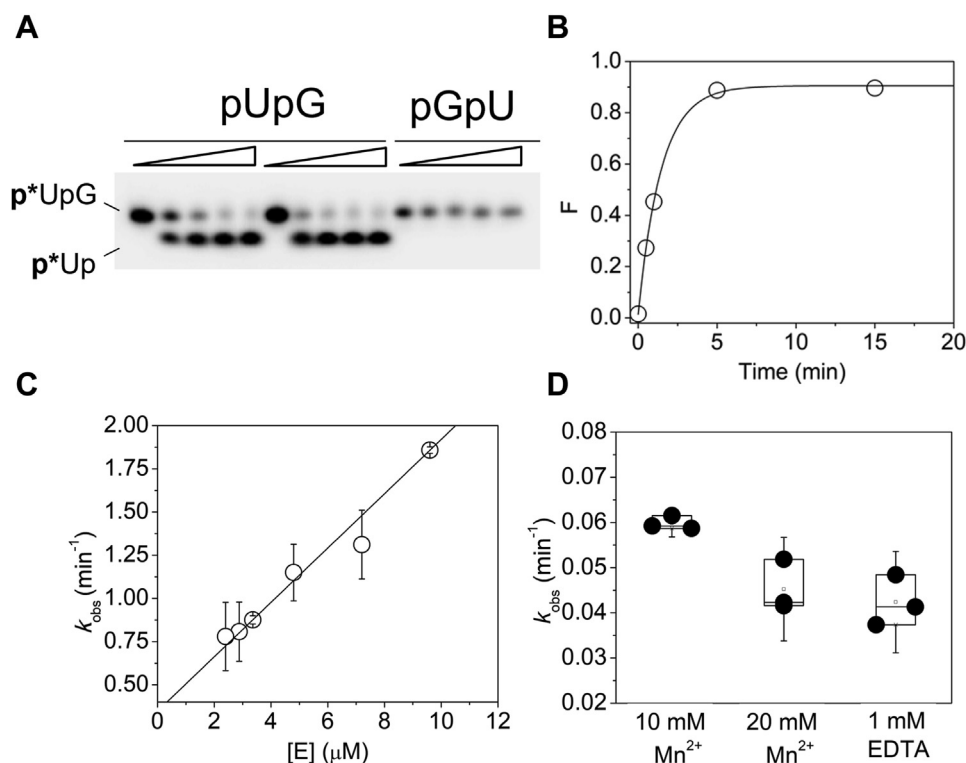

Figure 6. Single-turnover kinetics of pUpG dinucleotide cleavage by Nsp15 in the presence and absence of Mn^{2+}. *A*, analysis of 5′-^{32}P-pUpG and 5′-^{32}P-pGpU cleavage by denaturing PAGE. Time courses of Nsp15 reactions containing 0.5 μM Nsp15 and trace concentrations of ^{32}P-labeled substrate RNA in standard reaction buffer with 5 mM Mn^{2+}. *B*, plot showing fraction product formed (F = ([P]/([P] + [S])) *versus* time for pUpG cleavage in 5 mM Mn^{2+}. Data are fit to a single exponential function (*solid line*). *C*, plot showing the observed single-turnover rate constant k_{obs} *versus* Nsp15 concentration. The data are fit to a linear function with slope of *ca.* 2600 $M^{-1} s^{-1}$. *D*, comparison of k_{obs} for cleavage of 5′-^{32}P-pUpG at trace concentrations in reactions containing 5 μM Nsp15 and either 10 mM Mn^{2+}, 20 mM Mn^{2+}, or 1 mM EDTA. Nsp, nonstructural protein.
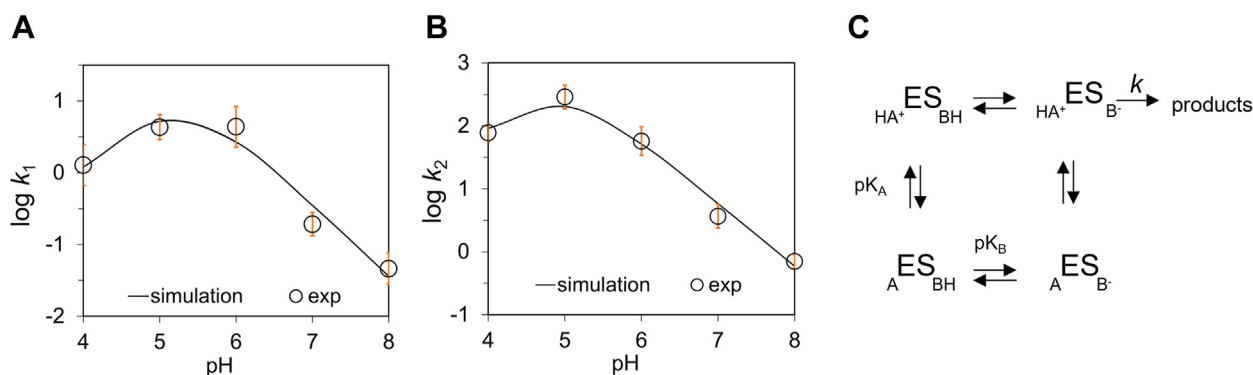
Figure 7. pH dependence of the rate constants for the slow (k_{obs1}) and fast (k_{obs2}) reaction phases for 1S cleavage by Nsp15. pH-rate profiles plotted as pH *versus* log k_{obs1} (*A*) and log k_{obs2} (*B*) measured by fitting kinetic to biphasic reaction model as described in the Experimental procedures section. *C*, equilibrium model for two ionizable active-site functional groups acting as an acid (HA:A+) and a base (BH:B−) involved in catalysis of RNA 2'-*O*-transphosphorylation with independent and noninteracting pK_a values of pK_A and pK_B for the acid and base, respectively. The data are fit to a rate equation based on the mechanism shown in *C* as described in the Experimental procedures section. Nsp, nonstructural protein.

pH dependence of Nsp15 cleavage of the dinucleotide substrate, we turned to multiple-turnover kinetics (Fig. 8). We used a previously established HPLC assay that permits all reaction products to be distinguished, and, as described later, this method enables quantification of the effects of substrate functional group modifications. The identities of the substrate and product peaks were previously established by analytical standards and mass spectrometry (46, 47). The reaction products from multiple-turnover reactions (74 μM UpG,

0.1 μM Nsp15) demonstrate catalysis of RNA 2'-*O*-transphosphorylation with no evidence of hydrolysis to form 2' or 3' UMP products consistent with rapid dissociation of the 2',3'-cyclic UMP product (Fig. 8*A*). The kinetics of product formation were linear, and the observed rate (v_{obs}) was identical in the presence of 1 mM EDTA and 5 mM Mn^{2+} (Fig. 8*B*). The v_{obs} for UpG cleavage increases linearly up to a concentration of 1300 μM consistent with the apparent weak binding observed in single-turnover experiments. Fitting the data to a
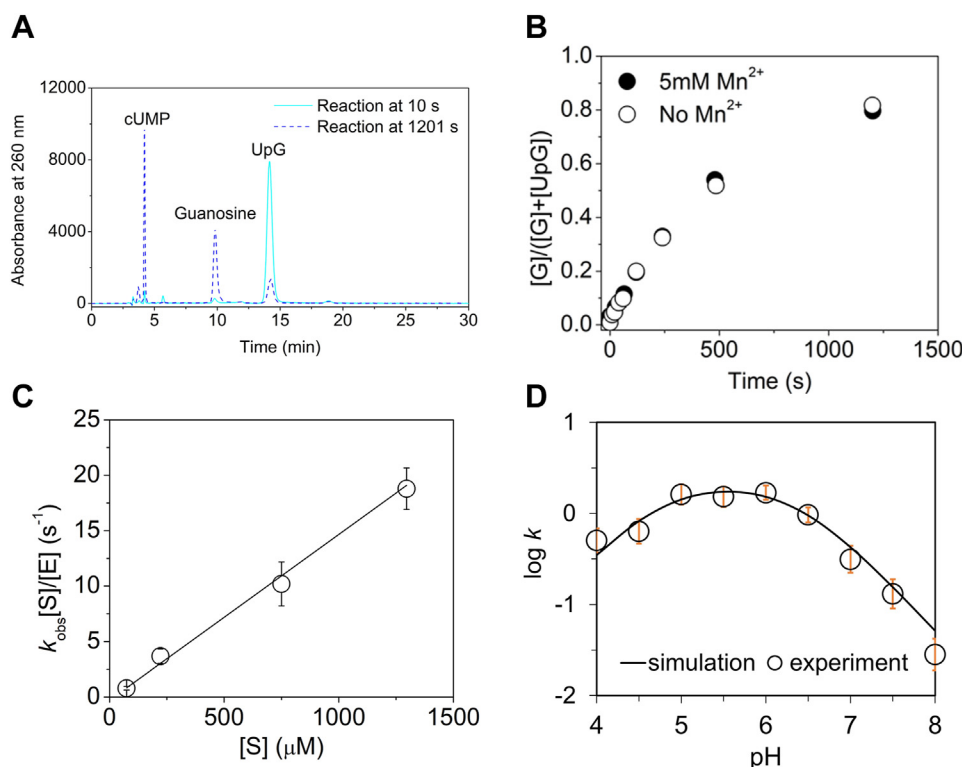

Figure 8. Multiple-turnover kinetics of Nsp15 cleavage of UpG dinucleotide RNA substrate and analysis of pH dependence of k_{cat}/K_m. *A*, reverse-phase HPLC (RP-HPLC) chromatogram of time points from a multiple-turnover reaction containing 74 μM UpG and 100 nM Nsp15 in standard reaction buffer pH 7.0. Time points correspond to 0 min (*solid line*) and 20 min (*dashed line*). The migration of UpG and cleavage products guanosine and cUMP is labeled. *B*, time course of product accumulation for multiple-turnover reactions of UpG in the presence of 5 mM Mn^{2+} (*filled circles*) or 1 mM EDTA (*open circles*). *C*, concentration dependence of the steady-state reaction velocity k_{obs}. The data are fit to a linear function with slope 1.5×10^4 M^{-1} s^{-1}. *D*, pH dependence of log k for multiple-turnover cleavage of UpG. The data are fit to an equation describing the dependence of active enzyme concentration according to the scheme shown for Figure 7*C*. cUMP, cyclic uridine monophosphate; Nsp, nonstructural protein.

linear equation yields a k_{cat}/K_m of 1.5×10^4 M^{-1}s^{-1} in the absence of Mn^{2+} (Fig. 8C). This value contrasts with the observed k_{cat}/K_m of 3.5×10^6 M^{-1}s^{-1} for RNase A cleavage of UpA and 1×10^6 M^{-1}s^{-1} for RNase T1 cleavage of GpU (34, 35). We determined the pH dependence of k_{cat}/K_m for Nsp15 cleavage of UpG by measuring v_{obs} at 74 µM substrate. The pH-rate profile for k_{cat}/K_m is bell shaped like the pH dependence of the single-turnover rate constants measured for the 1S substrate in 5 mM Mn^{2+} (Fig. 8D). The data fit to the same general model in which two functional groups on the enzyme contribute to k_{cat}/K_m as either an acid or a base with apparent p$K_{a,A}$ and p$K_{a,B}$ values of 4.8 and 6.4, respectively.

Thio effects on Nsp15 binding and cleavage are consistent with a mechanism involving an anionic transition state

The effects of phosphorothioate modifications can provide information on whether RNA 2'-*O*-transphosphorylation reactions proceed by an anionic transition state or involves protonation of a nonbridging oxygen in a triester-like mechanism. Gaining this insight is important because it helps define the possible roles of active-site ionizable groups in transition state stabilization. Interpretation of thio effects is based on the relative reactivities of phosphate *versus* phosphorothioate diesters and triesters in nonenzymatic reactions as well as the differential proton affinities of oxygen and sulfur (48–51). A large thio effect is predicted for either phosphorothioate stereoisomer for mechanisms involving protonation of a nonbridging oxygen, whereas small thio effects would be consistent with expectations for a mechanism involving an anionic transition state (Fig. S3).

Previous studies of Nsp15 thio effects demonstrated large effects on the apparent rate constant for cleavage of a substrate containing a mixture of *Rp* and *Sp* phosphorothioate stereoisomers (26). Yet, the stereochemistry of these effects was not established, and quantitative effects of modification were not documented. We purified the isomers of Up(s)G using reverse-phase (RP)-HPLC and measured their effect in single-

and multiple-turnover reactions (Fig. 9). Under single-turnover conditions (1.92 µM Nsp15, pH 8.0), the *Rp* isomer is readily cleaved with a k_{obs} of 0.22 min^{-1}, whereas the unmodified pUpG has a k_{obs} of 0.39 min^{-1} (Fig. 9, *B* and *C*). In contrast, the *Sp* isomer did not form product even after extended incubation. Thus, under single-turnover conditions, the thio effect (k_O/k_S) is at most twofold for the *Rp* phosphorothioate modification, whereas the *Sp* isomer reduces k_{obs} by an estimated >100-fold. Since the mechanistic impact of sulfur substitution impacts reaction rate regardless of which nonbridging oxygen is modified (48), this result is most consistent with a mechanism similar to nonenzymatic reactions catalyzed by base and RNase A involving an anionic transition state (52–54).

Given the apparently large effect of *Sp* phosphorothioate modification, we reasoned that the larger sulfur atom may result in weaker or altered binding. To test this hypothesis, we tested whether *Sp*-UpG acts as a competitor for binding of the active unmodified UpG substrate in multiple-turnover reactions. Reactions containing 100 µM UpG and 100 µM of either *Rp*-Up(s)G or *Sp*-Up(s)G were analyzed by RP-HPLC, and the depletion of both native and modified substrates and formation of the cUMP and uridine-2',3'-cyclic-phosphorothioate (cUMPS) products was quantified. Both Up(s)G stereoisomers have significantly slower retention times compared with UpG as does the cUMPS product compared with cUMP (Fig. 10A). A small amount of UMPS product was detected in the reaction containing *Rp*-Up(s)G in competition with the UpG substrate, consistent with a *ca.* 10-fold greater k_{cat}/K_m for the unmodified substrate. For the reaction containing *Sp*-Up(s)G, the only product detected was for the reaction of UpG, which indicates a k_{cat}/K_m for the Sp phosphorothioate–modified substrate that is smaller than for *Rp*-Up(s)G (Fig. 10, *B* and *C*).

Discussion

To resolve the details of the catalytic mechanism of Nsp15, roles of metal ion cofactors, substrate specificity, and effects of
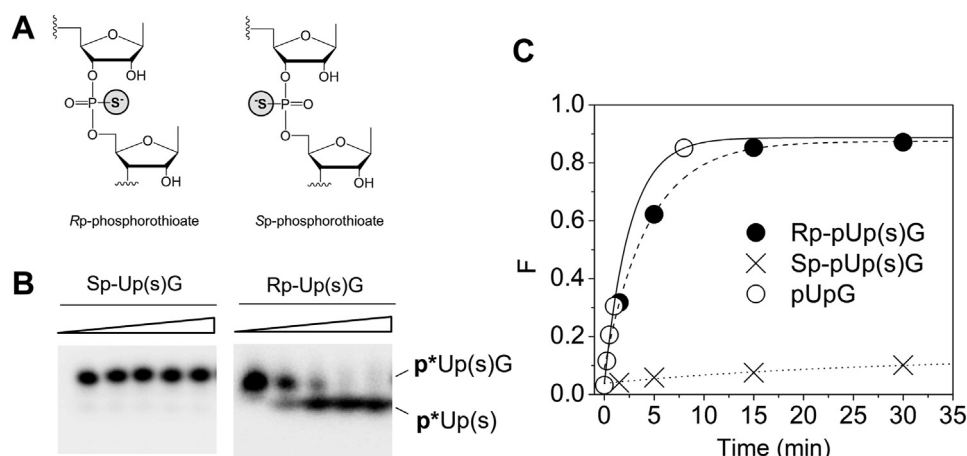

Figure 9. Effect of phosphorothioate modification on the single-turnover kinetics (k_c/k_s) of pUpG cleavage by Nsp15. *A, Rp* and *Sp* phosphorothioate stereoisomers. *B,* analysis of Nsp15 cleavage of 5'-^{32}P-*Sp*-pUpG and 5'-^{32}P-*Rp*-pGpU, containing a stereospecific sulfur modification at the scissile phosphate as indicated. Time courses of Nsp15 reactions containing 0.5 µM Nsp15 and trace concentrations of ^{32}P-labeled substrate RNA in standard reaction buffer with 5 mM Mn^{2+}. *C,* plot showing the kinetics of product formation (F=[P]/([P] + [S])) for Nsp15 cleavage of the unmodified 5'-^{32}P-pUpG substrate (*open circles, solid line*), 5'-^{32}P-*Rp*-pUpG (*filled circles, dashed line*), and 5'-^{32}P-*Sp*-pGpU (Xs, *dotted line*). Nsp, nonstructural protein.
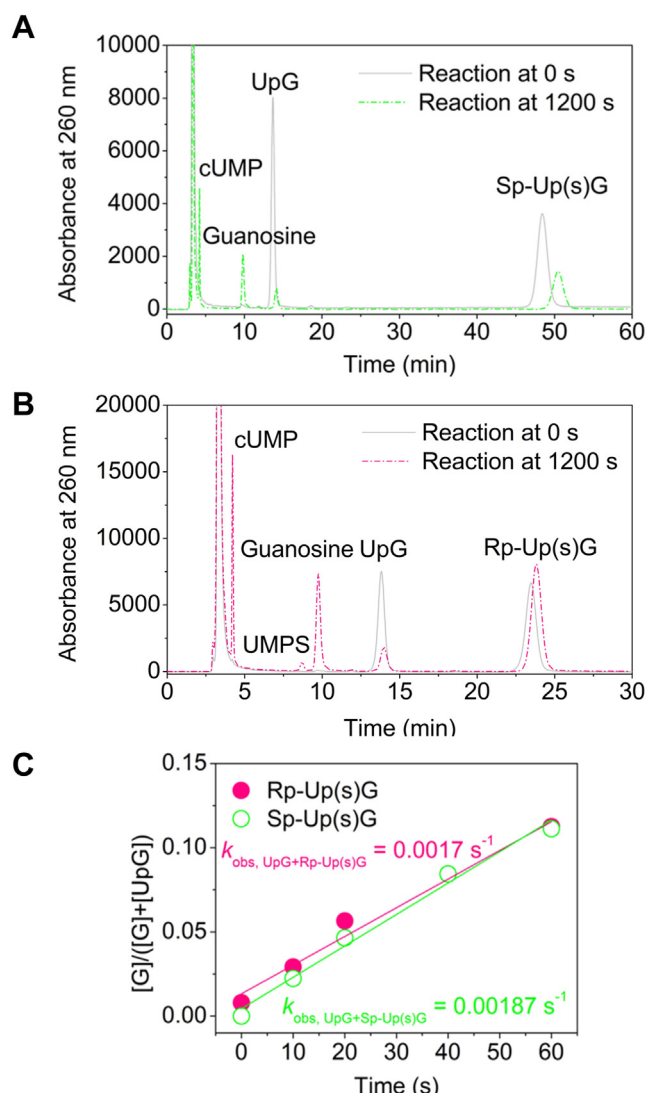
A

B

C

Figure 10. Effects of phosphorothioate modification on the multiple-turnover kinetics of UpG cleavage by Nsp15. *A*, analysis of the products of multiple-turnover reaction of Nsp15 containing 100 μM of either UpG (*solid line*) or *Sp*-Up(s)G (*dotted line*). The identity of peaks corresponding to substrates and products is indicated. *B*, analysis of the products of multiple-turnover reaction of Nsp15 containing 100 μM of either UpG (*solid line*) or *Rp*-Up(s)G (*dotted line*). The identity of peaks corresponding to substrates and products is indicated. *C*, kinetics of product formation for Nsp15 multiple-turnover reactions containing 100 mM UpG and an additional 100 mM *Rp*-Up(s)G (*filled circles*) or *Sp*-Up(s)G (*open circles*) as competitor. Nsp, nonstructural protein.

association with other Nsps, a quantitative mechanistic framework is required. Here, we used single- and multiple-turnover kinetics to provide kinetic evidence necessary to establish the catalytic mechanism of Nsp15. We compared rates of catalysis for three alternative substrates and quantified the contribution of Mn^{2+} to catalysis. The results establish an acid–base catalytic mechanism and further demonstrate that metal ion activation is substrate dependent. Interestingly, the kinetic data provide evidence that Mn^{2+} activates catalysis by stabilizing alternative enzyme states with faster rates of substrate cleavage on the enzyme. This observation suggests that metal ion activation, while dispensable for catalysis, may play a role in regulation depending on the cellular context of Nsp15

or its interactions with other Nsps. The occurrence of a ribonuclease enzymatic function in the RTC is unclear given that nonspecific or unregulated activity would obviously be detrimental to accumulation of functionally important viral RNAs. However, the potential to modulate the catalytic activity of Nsp15 indirectly by ion binding may provide a means to direct its activity toward specific targets or preferentially react with substrate RNAs at specific cellular loci.

The pH dependence of the cleavage reactions for oligonucleotide and dinucleotide substrates is a key observation that supports an acid–base catalytic mechanism. The two active-site histidine residues (H250 and H235) are the primary candidates for the titratable groups responsible for the observed pH-rate profiles for both the slow and fast reaction channels observed for oligonucleotide substrates. The conserved active-site residues K290, T341, and Y343 are also positioned adjacent to the reactive phosphoryl group; however, they are likely to have pK_A values that are significantly higher than the ∼pH 5 to 6 plateau and remain protonated across the entire pH-rate profile. Therefore, the observed pH-rate profiles cannot distinguish a mechanism involving an additional active-site acid with high p$K_{a,A}$ or alternatively a base with p$K_{a,B}$ outside the measurable range (42, 55, 56). Divalent metal ions can also contribute to pH dependence as acid–base catalysts *via* coordinated water molecules, as proposed for ribozyme-catalyzed RNA 2′-*O*-transphosphorylation (57). A hydrated metal ion acting as a general base could contribute to the observed pH-rate profile since the concentration of the active deprotonated form would increase as pH increases. However, a metal ion hydrate with a high pK_a acting as a general acid would be unlikely to contribute to the pH-rate profile and therefore cannot be excluded for the reaction in Mn^{2+} (58, 59). However, the observation that both the fast and slow reaction phases observed for the 1S substrate have similar pH-rate profiles, and the relatively small enhancement of reaction rate together is consistent with ES and E′S in Figure 5 employing the same mechanistic strategies.

The effects of *R*p and *S*p phosphorothioate modification on Nsp15 multiple turnover are generally consistent with previous studies, and the results from single-turnover experiments with the largest effect were observed for Sp modification. Even so, the effect of *R*p modification on k_{cat}/K_m is greater for the multiple-turnover reaction compared with the second-order rate constant for the single-turnover reaction k_c/K_s. This difference in the impact of phosphorothioate modification is likely to be due to a difference in the rate-limiting step for these two assays. If either phosphorothioate containing substrate bound tightly but reacted slowly or was unable to react, it would act in this assay as a competitive inhibitor. Therefore, this result is consistent with significantly weaker binding for the *S*p-Up(s)G and *R*p-Up(s)G than UpG because of the sulfur modification. The larger effect on Nsp15 cleavage because of *S*p phosphorothioate modification is consistent with structure models that position the *pro-S*p nonbridging phosphoryl oxygen deep in the active site (Fig. 11).

The biochemical activities and biophysical properties of SARS-CoV-2 Nsps ultimately define their roles in the viral life

cycle. Nsp15 is one of the least understood of the Nsps, and the connections between its substrate specificity, mechanism, and function are important to delineate. The quantitative functional data provide experimental support for several fundamentally important features of the Nsp15 active site and catalytic mechanism. Results from single-turnover kinetics establish that divalent metal ions are dispensable for Nsp15 catalysis and provide evidence that Mn^{2+} enhances the observed rate of cleavage by stabilizing alternative states of the ES complex. Based on recent structural studies by serial femtosecond crystallography using an X-ray free-electron laser and cryo-EM structures of free and bound enzyme, Jernigan *et al.* (60) proposed a model in which substrate binding alternates between the two trimers in the hexamer. In this reaction scheme, RNA binds with high affinity to one trimer, whereas the other trimer is more flexible. Thus, the fast- and slow-reaction phases observed in single-turnover reactions with oligonucleotide substrates may well reflect the differential flexibility of active sites in the Nsp15 hexamer. Nonetheless, the pH-rate profiles for both reaction phases for oligonucleotide and dinucleotide substrates are characteristic of an acid–base catalytic mechanism, and Mn^{2+} has no observable effect on pH dependence, further supporting a noncatalytic role in rate enhancement. The orientations of H250 and H235 are consistent with roles as base and acid, respectively, whereas K290 provides electrostatic stabilization for the anionic transition state analogous to the roles of H12, H119, and K41 in RNase A. These features suggest that inhibitor design might take advantage of the late associative transition state established for nonenzymatic and ribonuclease-catalyzed reactions. On the other hand, the importance of maintaining oxygens at

Figure 11. Active-site model for Nsp15 based on dinucleotide complex (Protein Data Bank: 7N33). The positions of stereospecific phosphorothioate modifications are indicated. The location of the pro-Sp nonbridging oxygen at which sulfur substitution has a large effect on binding is highlighted in *yellow*. The active-site residues implicated in catalysis (K290, H235, and 0H350) are labeled, and the residue S294 is involved in uridine nucleobase recognition. Nsp, nonstructural protein.

the nonbridging positions of the diester precludes the use of phosphorothioate analogs as competitive inhibitors.

Experimental procedures

Nsp15 cloning, expression, and purification

The sequence of the SARS-CoV-2 Nsp15 protein (NF039890.1) was codon optimized for *Escherichia coli* K12 with the online Integrated DNA Technologies tool. A gene block was commercially synthesized (Integrated DNA Technologies) and subsequently inserted into the pMCSG7vector by ligation-independent cloning (61). Recombinant protein was overexpressed in T7 express–competent *E. coli* cells (NEB) grown in Terrific broth supplemented with 100 µg/ml ampicillin at 37 °C and 190 rpm (62). At an absorbance of 1 at 600 nm, Nsp15 expression was initiated by addition of 0.2 mM IPTG; after induction, the cultures were cooled to 18 °C and grown for an additional 20 h. Cells were recovered by centrifugation, and cell pellets were stored at –80 °C. For purification, cell pellets were resuspended in lysis buffer (50 mM Hepes [pH 8], 500 mM NaCl, 20 mM imidazole, 5% glycerol, and 10 mM β-mercaptoethanol), and a cell disrupter was utilized to lyse cells. Cells were lysed at 4 °C under continuous flow at a pressure of 23 to 27 kPsi. Cellular debris was removed by centrifugation at 19,000 rpm for 1 h at 4 °C in a Beckman JLA 4.1 rotor. After centrifugation, the lysate was filtered using 0.45 µm syringe filters and loaded onto two stacked 1 ml Histrap columns (Cytiva) using an AKTA GO chromatography system. The column was washed with wash buffer (50 mM Hepes [pH 8], 500 mM NaCl, 10 mM imidazole, 5% glycerol, and 10 mM β-mercaptoethanol), and Nsp15 was eluted by gradient of wash and elution buffer (50 mM Hepes [pH 8], 500 mM NaCl, 500 mM imidazole, 5% glycerol, and 10 mM β-mercaptoethanol). Eluted Nsp15 fractions were concentrated by Millipore 30 kDa centrifuge filters and buffer exchanged into lower salt (50 mM Hepes [pH 8] and 300 mM NaCl). Heximeric Nsp15 was further purified by size-exclusion chromatography (GE HiLoad 16/600 Superdex 200 pg) in Nsp15 size-exclusion buffer buffer (50 mM Hepes [pH 8], 300 mM NaCl, 5% glycerol, and 1 mM β-mercaptoethanol). Again, eluted Nsp15 fractions were concentrated by Millipore 30 kDa centrifuge filters. Pure Nsp15 stocks were stored in 50% glycerol at –80 °C.

CD and fluorescence spectroscopy

CD data were acquired on an Applied Photophysics Chirascan spectrometer. Nsp15 (0.46 µM) was prepared in 2 mM Hepes,100 mM KCl, and 5 mM MnCl and transferred to a 2 mm quartz cell at room temperature. Samples were scanned from 200 to 280 nm with a bandwidth and step size of 1 nm. This was repeated for Nsp15 in buffer lacking MgCl₂. Intrinsic tryptophan fluorescence spectra were acquired on an Agilent Carey Eclipse fluorescence spectrometer using the "scan mode" of the Carey Eclipses WinFLR software. Nsp15 (0.5 µM) was prepared in buffer (250 mM Hepes [pH 8] and 500 mM KCl) in a 0.7 × 0.7 cm quartz cuvette. Scan settings include an excitation wavelength of 295 nm, emission scan from 310 to 400 nm, slit width of 5 nm, and CAT mode of five scan
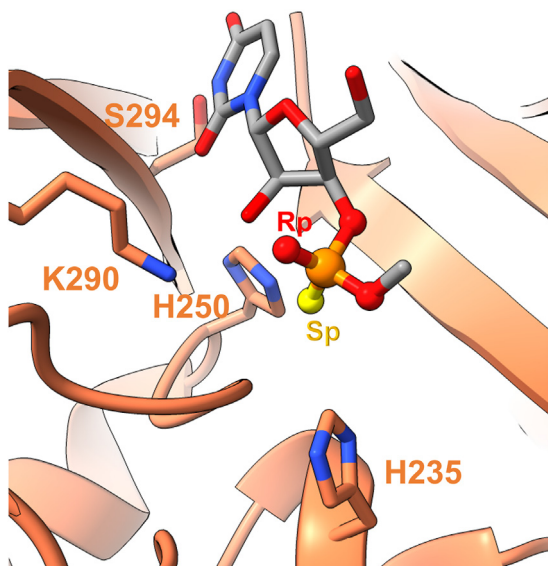
averaging. Mn^{2+} was titrated in 2 µl increments from a 1 M stock of MnCl until the peak no longer decreased. Maximum emission was approximately 340 nm.

Analysis of in vitro Nsp15 cleavage kinetics

Substrates were obtained commercially (Horizon Discovery) and deprotected according to the manufacturer's protocol. The sequences of the substrates PUN, 1S, and 5′-pUpG-3′ are listed in Table 1. The concentrations of stock solutions were determined by UV spectroscopy using the following extinction coefficients (PUN, 298,602 l/mol·cm; 1S, 212,330 l/mol·cm; and UpG, 20,000 l/mol·cm). The 1S substrate was synthesized to contain a 5′ Cy3 label, and the PUN substrate contained 5′-Cy5 and 3′-TAMRA labels. UpG was 5′ end labeled with ^{32}P using T4 polynucleotide kinase (NEB) and [γ-^{32}P]ATP (PerkinElmer). Labeling reactions were incubated at 37 °C for 1 h in a reaction containing 1× polynucleotide kinase buffer (NEB), 0.1 µmole RNA, 400 pmol of [γ-^{32}P]ATP, 100 units of superasin, and 80 units of T4 polynucleotide kinase in a total volume of 200 µl. The RNA was recovered by gel purification and quantified by isotopic counting.

Single-turnover reactions were set up at pH 8 and 25 °C. The substrate concentration was <2 nM. The reaction buffer consisted of 50 mM Hepes/Pipes, 5 mM manganese chloride, 0.1 M potassium chloride, and 1 mM DTT. Enzyme and substrate tubes were prepared, incubated at 25 °C for 5 min, and mixed to initiate the reaction. Individual time points were collected by stopping the reactions with 1:1.5 volume of formamide loading dye. Reaction time points were run on a 20% polyacrylamide gel for 150 min at 110 V. The gel was then dried in a gel dryer onto Whatman filter paper. Phosphor screen was exposed to the gel and scanned in Amersham Typhoon scanner. ImageQuant (Cytiva) was used to determine the relative densities of the substrate and product bands, and these were fit to the first-order rate equation:

$$Y = Ae^{\wedge}(-kt)^{-kt} + B$$

Several different reaction buffers were prepared with different concentrations of manganese chloride.

Analysis of pH dependence of Nsp15 cleavage

The 1S substrate was obtained commercially and deprotected using the manufacturer's protocol. Single-turnover reactions were performed using 500 nM enzyme and 50 nM substrate (E/S >10) in a buffer containing 50 mM NaOAc/Mes/Hepes with a range of pHs from 4 to 8, 0.1 M KCl, 5 mM $MnCl_2$, and 1 mM DTT. Enzyme and substrate were prepared, incubated at 25 °C for 15 min, and mixed to initiate the reaction. Samples were taken from the reaction tube at different time intervals from 10 s to 1 h. The reactions were stopped by adding an equal volume of a gel-loading buffer containing 90% formamide and 0.5 M EDTA. The reaction was run on 20% polyacrylamide gel for 2.5 h at 120 V and scanned using Amersham Typhoon Phosphorimager. The relative densities of the substrate and product bands were determined by using ImageJ, (NIH) and the relative fraction of reaction of the formation of product or the disappearance of the substrate with respect to time was fit to a double exponential rate equation:

$$Y = A_1 e^{\wedge(-xt_1)} + A_2 e^{\wedge(-xt_2)} + Y_0$$

The rate constants were calculated for each reaction at different pHs. The pH rate profile graph was made by plotting common logarithm of rate constants *versus* pH values. The pKa values for general acid and base were generated by fitting the observed rate constants to a general equation for two ionizable active-site groups acting as acid and base:

$$k = \frac{k_c}{\left(1 + 10^{(pK_{a,B} + pH)} + 10^{(pK_{a,B} - pK_{a,A})} + 10^{(pH - pK_{a,A})}\right)}$$

Multiple-turnover experiments were conducted in a buffer containing 50 mM NaOAc/Mes/Hepes with a range of pHs from 4 to 8, 0.1 M KCl, 1 mM DTT, and 1 mM EDTA at 25 °C. A multiple-turnover reaction of 74 µM UpG substrate and 0.1 µM Nsp15 at pH 7 was used to investigate the kinetics of the enzyme. After an incubation at 25 °C for 10 min, the reactions were initiated by combining equal volume of enzyme and substrate. Aliquots of the reaction mixture were taken at selected time points. One part of the reaction mixture was added to 1.5 parts of 7 M urea to quench the reaction. The remaining dinucleotide substrate and products in each aliquot were separated on a RP C18 column with a running buffer containing 0.1 M ammonium acetate and 3.5% acetonitrile. Fraction of product formed in each sample was quantified with peak areas using the equation below:

$$F = \frac{1.8 \times A_G}{A_{UpG} + 1.8 \times A_G}$$

where A_G is the peak area of guanosine, A_{UpG} is the peak area of UpG, and a constant equal to 1.8 is used to account for the difference of molar absorptivity between guanosine and UpG.

The observed initial rates (k_{obs}, in s^{-1}) of each reaction were estimated by fitting the first ~10% of product formation *versus* time to a linear function, where the slope represented the observed initial rate. The k_{obs} was then multiplied by substrate concentration and normalized to total enzyme concentration of the reaction to yield the initial multiple-turnover rate constant (k, in s^{-1}).

$$k = \frac{k_{obs} \times [S]}{[E]}$$

Reactions at every substrate concentration were triplicated. Averaged initial multiple-turnover rate constants were plotted *versus* substrate concentrations and fit to a linear function.

A multiple-turnover reaction of 74 µM UpG substrate and 50 nM Nsp15 was used to investigate the pH dependence of the enzyme with the HPLC-based assay as previously described

(46). Reactions at every pH were conducted in triplicate. Common logarithm of averaged initial multiple-turnover rate constants was plotted *versus* pHs. The averaged initial multiple-turnover rates were also fit to the general equation for two ionizable active-site groups acting as acid and base to yield the pK_a values for the general acid and general base.

Quantification of thio effects on Nsp15 cleavage of Up(s)G

The *Rp* and *Sp* diastereomers of UpSG were isolated by RP-HPLC (63). The *Rp* and *Sp* fractions from the different HPLC runs were pooled together and freeze dried. These were reconstituted in water and redried three times to remove buffer salts. The *Rp*- and *Sp*-Up(s)G RNAs were 5′-end labeled with ^{32}P as described, previously, for unmodified RNA. For competition studies, 100 mM *Rp*-Up(s)G or *Sp*-Up(s)G was added to a multiple-turnover reaction containing 74 mM UpG and 100 nM Nsp15 hexamer. Reactions were performed in a similar manner as described for multiple-turnover kinetics. The observed initial rates (k_{obs}, in s^{-1}) of UpG processing by Nsp15 were measured by fitting the first ~10% of guanosine accumulation *versus* time to a linear function, where the slope represented the observed initial rate.

Data availability

The authors declare that all data that support the findings of this study are available within this article and its accompanying files.

Conflict of interest—The authors declare that they have no conflicts of interest with the contents of this article.

Abbreviations—The abbreviations used are: cUMPS, uridine-2′,3′-cyclic-phosphorothioate; ES, enzyme–substrate; nsp, nonstructural protein; PUN, polyuridine negative-sense RNA; RP, reverse phase; RTC, replication–transcription complex; SARS-CoV-2, severe acute respiratory syndrome coronavirus 2; UMP, uridine monophosphate.

References

1. V'Kovski, P., Kratzel, A., Steiner, S., Stalder, H., and Thiel, V. (2021) Coronavirus biology and replication: implications for SARS-CoV-2. *Nat. Rev. Microbiol.* **19**, 155–170

2. Hartenian, E., Nandakumar, D., Lari, A., Ly, M., Tucker, J. M., and Glaunsinger, B. A. (2020) The molecular virology of coronaviruses. *J. Biol. Chem.* **295**, 12910–12934

3. Brant, A. C., Tian, W., Majerciak, V., Yang, W., and Zheng, Z. M. (2021) SARS-CoV-2: from its discovery to genome structure, transcription, and replication. *Cell Biosci.* **11**, 136

4. Malone, B., Urakova, N., Snijder, E. J., and Campbell, E. A. (2022) Structures and functions of coronavirus replication-transcription complexes and their relevance for SARS-CoV-2 drug design. *Nat. Rev. Mol. Cell Biol.* **23**, 21–39

5. Nishikiori, M., den Boon, J. A., Unchwaniwala, N., and Ahlquist, P. (2022) Crowning touches in positive-strand RNA virus genome replication complex structure and function. *Annu. Rev. Virol.* **9**, 193–212

6. Snijder, E. J., Limpens, R., de Wilde, A. H., de Jong, A. W. M., Zevenhoven-Dobbe, J. C., Maier, H. J., *et al.* (2020) A unifying structural and functional model of the coronavirus replication organelle: tracking down RNA synthesis. *PLoS Biol.* **18**, e3000715

7. Nencka, R., Silhan, J., Klima, M., Otava, T., Kocek, H., Krafcikova, P., *et al.* (2022) Coronaviral RNA-methyltransferases: function, structure and inhibition. *Nucl. Acids Res.* **50**, 635–650

8. Hillen, H. S. (2021) Structure and function of SARS-CoV-2 polymerase. *Curr. Opin. Virol.* **48**, 82–90

9. Frazier, M. N., Riccio, A. A., Wilson, I. M., Copeland, W. C., and Stanley, R. E. (2022) Recent insights into the structure and function of coronavirus ribonucleases. *FEBS Open Bio* **12**, 1567–1583

10. Yan, L., Yang, Y., Li, M., Zhang, Y., Zheng, L., Ge, J., *et al.* (2021) Coupling of N7-methyltransferase and 3′-5′ exoribonuclease with SARS-CoV-2 polymerase reveals mechanisms for capping and proofreading. *Cell* **184**, 3474–3485

11. Deng, X., Hackbart, M., Mettelman, R. C., O'Brien, A., Mielech, A. M., Yi, G., *et al.* (2017) Coronavirus nonstructural protein 15 mediates evasion of dsRNA sensors and limits apoptosis in macrophages. *Proc. Natl. Acad. Sci. U. S. A.* **114**, e4251–e4260

12. Deng, X., and Baker, S. C. (2018) An "Old" protein with a new story: coronavirus endoribonuclease is important for evading host antiviral defenses. *Virology* **517**, 157–163

13. Hackbart, M., Deng, X., and Baker, S. C. (2020) Coronavirus endoribonuclease targets viral polyuridine sequences to evade activating host sensors. *Proc. Natl. Acad. Sci. U. S. A.* **117**, 8094–8103

14. Frazier, M. N., Dillard, L. B., Krahn, J. M., Perera, L., Williams, J. G., Wilson, I. M., *et al.* (2021) Characterization of SARS2 Nsp15 nuclease activity reveals it's mad about U. *Nucl. Acids Res.* **49**, 10136–10149

15. Bhardwaj, K., Sun, J., Holzenburg, A., Guarino, L. A., and Kao, C. C. (2006) RNA recognition and cleavage by the SARS coronavirus endoribonuclease. *J. Mol. Biol.* **361**, 243–256

16. Ivanov, K. A., Hertzig, T., Rozanov, M., Bayer, S., Thiel, V., Gorbalenya, A. E., *et al.* (2004) Major genetic marker of nidoviruses encodes a replicative endoribonuclease. *Proc. Natl. Acad. Sci. U. S. A.* **101**, 12694–12699

17. Ulferts, R., and Ziebuhr, J. (2011) Nidovirus ribonucleases: structures and functions in viral replication. *RNA Biol.* **8**, 295–304

18. Ricagno, S., Egloff, M. P., Ulferts, R., Coutard, B., Nurizzo, D., Campanacci, V., *et al.* (2006) Crystal structure and mechanistic determinants of SARS coronavirus nonstructural protein 15 define an endoribonuclease family. *Proc. Natl. Acad. Sci. U. S. A.* **103**, 11892–11897

19. Frazier, M. N., Wilson, I. M., Krahn, J. M., Butay, K. J., Dillard, L. B., Borgnia, M. J., *et al.* (2022) Flipped over U: structural Basis for dsRNA cleavage by the SARS-CoV-2 endoribonuclease. *Nucl. Acids Res.* **50**, 8290–8301

20. Kim, Y., Wower, J., Maltseva, N., Chang, C., Jedrzejczak, R., Wilamowski, M., *et al.* (2021) Tipiracil binds to uridine site and inhibits Nsp15 endoribonuclease NendoU from SARS-CoV-2. *Commun. Biol.* **4**, 193

21. Pillon, M. C., Frazier, M. N., Dillard, L. B., Williams, J. G., Kocaman, S., Krahn, J. M., *et al.* (2021) Cryo-EM structures of the SARS-CoV-2 endoribonuclease Nsp15 reveal insight into nuclease specificity and dynamics. *Nat. Commun.* **12**, 636

22. Ancar, R., Li, Y., Kindler, E., Cooper, D. A., Ransom, M., Thiel, V., *et al.* (2020) Physiologic RNA targets and refined sequence specificity of coronavirus EndoU. *RNA* **26**, 1976–1999

ASBMB

J. Biol. Chem. (2023) 299(6) 104787 **11**

23. Jankowsky, E., and Harris, M. E. (2015) Specificity and nonspecificity in RNA-protein interactions. *Nat. Rev. Mol. Cell Biol.* **16**, 533–544

24. Mokhtari, D. A., Appel, M. J., Fordyce, P. M., and Herschlag, D. (2021) High throughput and quantitative enzymology in the genomic era. *Curr. Opin. Struct. Biol.* **71**, 259–273

25. Kim, Y., Jedrzejczak, R., Maltseva, N. I., Wilamowski, M., Endres, M., Godzik, A., *et al.* (2020) Crystal structure of Nsp15 endoribonuclease NendoU from SARS-CoV-2. *Protein Sci.* **29**, 1596

26. Bhardwaj, K., Palaninathan, S., Alcantara, J. M., Yi, L. L., Guarino, L., Sacchettini, J. C., *et al.* (2008) Structural and functional analyses of the severe acute respiratory syndrome coronavirus endoribonuclease Nsp15. *J. Biol. Chem.* **283**, 3655–3664

27. Xu, X., Zhai, Y., Sun, F., Lou, Z., Su, D., Xu, Y., *et al.* (2006) New antiviral target revealed by the hexameric structure of mouse hepatitis virus nonstructural protein nsp15. *J. Virol.* **80**, 7909–7917

28. Canal, B., Fujisawa, R., McClure, A. W., Deegan, T. D., Wu, M., Ulferts, R., *et al.* (2021) Identifying SARS-CoV-2 antiviral compounds by screening for small molecule inhibitors of nsp15 endoribonuclease. *Biochem. J.* **478**, 2465–2479

29. Bhardwaj, K., Guarino, L., and Kao, C. C. (2004) The severe acute respiratory syndrome coronavirus Nsp15 protein is an endoribonuclease that prefers manganese as a cofactor. *J. Virol.* **78**, 12218–12224

30. Zhang, L., Li, L., Yan, L., Ming, Z., Jia, Z., Lou, Z., *et al.* (2018) Structural and biochemical characterization of endoribonuclease Nsp15 encoded by Middle East respiratory syndrome coronavirus. *J. Virol.* **92**. https://doi.org/10.1128/JVI.00893-18

31. McNaughton, R. L., Reddi, A. R., Clement, M. H., Sharma, A., Barnese, K., Rosenfeld, L., *et al.* (2010) Probing in vivo Mn^{2+} speciation and oxidative stress resistance in yeast cells with electron-nuclear double resonance spectroscopy. *Proc. Natl. Acad. Sci. U. S. A.* **107**, 15335–15339

32. Bowman, A. B., and Aschner, M. (2014) Considerations on manganese (Mn) treatments for *in vitro* studies. *NeuroToxicology* **41**, 141–142

33. Johnson, K. A., and Sigman, D. S. (1992) *Transient-State Kinetic Analysis of Enzyme Reaction Pathways in the Enzymes*. In The Enzymes, Academic Press, New York: 1–61

34. Park, C., and Raines, R. T. (2003) Catalysis by ribonuclease A is limited by the rate of substrate association. *Biochemistry* **42**, 3509–3518

35. Loverix, S., Winqvist, A., Strömberg, R., and Steyaert, J. (2000) Mechanism of RNase T1: concerted triester-like phosphoryl transfer via a catalytic three-centered hydrogen bond. *Chem. Biol.* **7**, 651–658

36. Lakowicz, J. (1999) *Principles of Fluoresence Spectroscopy*, Kluwer, New York

37. Royer, C. A. (2006) Probing protein folding and conformational transitions with fluorescence. *Chem. Rev.* **106**, 1769–1784

38. Greenfield, N. J. (2006) Using circular dichroism spectra to estimate protein secondary structure. *Nat. Protoc.* **1**, 2876–2890

39. Wolfenden, R. (2011) Benchmark reaction rates, the stability of biological molecules in water, and the evolution of catalytic power in enzymes. *Annu. Rev. Biochem.* **80**, 645–667

40. Wolfenden, R., Ridgway, C., and Young, G. (1998) Spontaneous hydrolysis of ionized phosphate monoesters and diesters and the proficiencies of phosphatases and phosphodiesterases as catalysts. *J. Am. Chem. Soc.* **120**, 833–834

41. Harris, M. E., York, D. M., Piccirilli, J. A., and Anderson, V. E. (2017) Kinetic isotope effect analysis of RNA 2'-O-transphosphorylation. *Met. Enzymol.* **596**, 433–457

42. Cleland, W. W., and Cook, P. (2007) In *pH Dependence of Kinetic Parameters and Isotope Effects in Enzyme Kinetics and Mechanism*, Garland Science, New York

43. Eftink, M. R., and Biltonen, R. L. (1983) Energetics of ribonuclease A catalysis. 1. pH, ionic strength, and solvent isotope dependence of the

44. Herries, D. G., Mathias, A. P., and Rabin, B. R. (1962) The active site and mechanism of action of bovine pancreatic ribonuclease. 3. The pH-dependence of the kinetic parameters for the hydrolysis of cytidine 2',3'-phosphate. *Biochem. J.* **85**, 127–134

hydrolysis of cytidine cyclic 2',3'-phosphate. *Biochemistry* **22**, 5123–5134

45. Findlay, D., Herries, D., Mathias, A., Rabin, B., and Ross, C. (1962) The active site and mechanism of action of bovine pancreatic ribonuclease. 7. The catalytic mechanism. *Biochem. J.* **85**, 152

46. Harris, M. E., Dai, Q., Gu, H., Kellerman, D. L., Piccirilli, J. A., and Anderson, V. E. (2010) Kinetic isotope effects for RNA cleavage by 2'-O-transphosphorylation: nucleophilic activation by specific base. *J. Am. Chem. Soc.* **132**, 11613–11621

47. Harris, M. E., York, D., Piccirilli, J. A., and Anderson, V. E. (2017). In *Kinetic Isotope Effect Analysis of RNA 2'-O-Transphosphorylation in Methods in Enzymology*, CRC Press, New York

48. Herschlag, D. (1994) Ribonuclease revisited: catalysis *via* the classical general acid-base mechanism or a triester-like mechanism? *J. Am. Chem. Soc.* **116**, 11631–11635

49. Eckstein, F. (1985) Nucleoside phosphorothioates. *Annu. Rev. Biochem.* **54**, 367–402

50. Lönnberg, H. (2022) Structural modifications as tools in mechanistic studies of the cleavage of RNA phosphodiester linkages. *Chem. Rec.* **22**, e202200141

51. Frey, P. A., and Sammons, R. D. (1985) Bond order and charge localization in nucleoside phosphorothioates. *Science* **228**, 541–545

52. Oivanen, M., Kuusela, S., and Lonnberg, H. (1998) Kinetics and mechanisms for the cleavage and isomerization of the phosphodiester bonds of RNA by Bronsted acids and bases. *Chem. Rev.* **98**, 961–990

53. Raines, R. T. (1998) Ribonuclease A. *Chem. Rev.* **98**, 1045–1065

54. Gu, H., Zhang, S., Wong, K. Y., Radak, B. K., Dissanayake, T., Kellerman, D. L., *et al.* (2013) Experimental and computational analysis of the transition state for ribonuclease A-catalyzed RNA 2'-O-transphosphorylation. *Proc. Natl. Acad. Sci. U. S. A.* **110**, 13002–13007

55. Bevilacqua, P. C. (2003) Mechanistic considerations for general acid-base catalysis by RNA: revisiting the mechanism of the hairpin ribozyme. *Biochemistry* **42**, 2259–2265

56. Kath-Schorr, S., Wilson, T. J., Li, N. S., Lu, J., Piccirilli, J. A., and Lilley, D. M. (2012) General acid-base catalysis mediated by nucleobases in the hairpin ribozyme. *J. Am. Chem. Soc.* **134**, 16717–16724

57. Lilley, D. M. J. (2019) Classification of the nucleolytic ribozymes based upon catalytic mechanism. *F1000Res.* **8**, 1462

58. Cortés-Guajardo, C., Rojas-Hernández, F., Paillao-Bustos, R., and Cepeda-Plaza, M. (2021) Hydrated metal ion as a general acid in the catalytic mechanism of the 8-17 DNAzyme. *Org. Biomol. Chem.* **19**, 5395–5402

59. Wilson, T. J., Liu, Y., Li, N. S., Dai, Q., Piccirilli, J. A., and Lilley, D. M. J. (2019) Comparison of the structures and mechanisms of the pistol and hammerhead ribozymes. *J. Am. Chem. Soc.* **141**, 7865–7875

60. Jernigan, R. J., Logeswaran, D., Doppler, D., Nagaratnam, N., Sonker, M., Yang, J.-H., *et al.* (2023) Room-temperature structural studies of SARS-CoV-2 protein NendoU with an X-ray free-electron laser. *Structure* **31**, 138–151.e5

61. Eschenfeldt, W. H., Lucy, S., Millard, C. S., Joachimiak, A., and Mark, I. D. (2009) A family of LIC vectors for high-throughput cloning and purification of proteins. *Met. Mol. Biol.* **498**, 105–115

62. Sambrook, J., Fritsch, E. F., and Maniatis, T. (1989) *Molecular Cloning: A Laboratory Manual*, Cold Spring Harbor Laboratory Press, Cold Spring Harbor, NY

63. Frederiksen, J. K., and Piccirilli, J. A. (2009) Separation of RNA phosphorothioate oligonucleotides by HPLC. *Met. Enzymol.* **468**, 289–309

ASBMB